Influence of the Ageing and Drying Steps of a CoMoP/γ-Al2O3 Catalyst onto the Multi-Scale Molybdenum Active Phase Organization

Candice Cottrez, Séverine Humbert, Anne-sophie Gay, Elodie Devers, Frédéric de Geuser, Xavier Carrier, Alexandra Chaumonnot

ChemCatChem

Research Article
doi.org/10.1002/cctc.202201432

Chemistry Europe
European Chemical Societies Publishing

www.chemcatchem.org

Special Collection

Influence of the Ageing and Drying Steps of a CoMoP/γ-Al_2O_3 Catalyst onto the Multi-Scale Molybdenum Active Phase Organization

Candice Cottrez,[a] Séverine Humbert,[a] Anne-Sophie Gay,*[a] Elodie Devers,[a] Frédéric De Geuser,[b] Xavier Carrier,[c] and Alexandra Chaumonnot[a]

To study the influence of ageing and drying steps onto the multiscale Mo active phase arrangement (*i.e.* MoS_2 slabs and slab aggregates), a series of highly loaded CoMoP/γ-Al_2O_3 catalysts aged, unaged, dried or freeze-dried were prepared and tested in toluene hydrogenation. Electron Probe Micro Analyses (EPMA) and Anomalous Small Angle X-Ray Scattering (ASAXS) permit to highlight the influence of each preparation steps. A growth of Mo entities occurs during ageing along with metal diffusion inside the support and leads to longer slabs. The same occurs during drying with metal redistribution due to solvent evaporation. Concomitantly, a fragmentation of slab aggregates takes place and leads to numerous small slabs aggregates. Slab length and aggregates amount were found to drive the catalytic activity, which translates the relationship between activity, number of active sites and their accessibility. Conversely, macroscopic metal distribution into the extrudates appears to have no impact on the catalytic performance.

Introduction

For last decades, strict standards have imposed a very low sulfur content in fuels (less than 10 ppm since 2009 in Europe) because of its toxicity and its ability to produce SOx pollutants. These criteria lead to the design of ever more efficient hydrotreating catalysts. The simplest way to obtain more active catalysts is to increase the amount of active phase. However, the increase of the intrinsic activity (catalytic activity per metal atom) is limited at high metal contents. At too high metal content, it can even be detrimental for the catalytic performance as was first demonstrated by Platanitis *et al.*[1] for Mo/TiO_2 catalysts with a d(Mo) > 4 at (Mo)/nm^2, and then subsequently observed for other systems.[2–4] Therefore, the preparation of intrinsically more active catalysts, allowing to improve their efficiency, is a rational way to improve existing catalysts.

Catalysts used for hydrodesulfurization reactions (HDS) are composed of MS_2 slabs (M being a group VIB transition metal: Mo, W), promoted by a group VIII transition metal (Co, Ni) and dispersed on the surface of a shaped porous material (*e.g.* alumina or titanium dioxide extrudates). These slabs are obtained by sulfidation of oxide phases obtained after deposition and drying of the associated metal precursors on the surface of the chosen support.[5] Thus, the catalytic activity of a CoMoP/γ-Al_2O_3 type catalyst is due to cobalt-promoted MoS_2 slabs a few nm long.[5,6] More precisely, the active sites of HDS reactions have been attributed to "mixed sites" so-called CoMoS. The presence of such sites has been demonstrated by in situ Mössbauer spectroscopy or by NO adsorption followed by infrared (IR) spectroscopy.[7,8] Furthermore, MoS_2 slabs are well described in the literature through X-ray photoelectron spectroscopy (XPS) and transmission electron microscopy (TEM) analyses. Indeed, the sulfidation rate, the promotion degree, the stacking level and the slabs length have a direct influence on the nature and number of mixed sites which are directly correlated to the intrinsic activity as it has been shown by Gandubert *et al.*[9] The loss of intrinsic activity observed by Platanitis[1] at high Mo loading could then be explained by a decrease in the dispersion of the active phase,[10] parameter that depends on the slabs length and the sulfidation degree[7] or by pore blocking effect.[11] Besides, a recent study[12] revealed the presence of slabs aggregates of a few tens of nanometers by High Angle Annular Dark Field Scanning Transmission Electron Microscopy (HAADF-STEM). Thus, characterizing only the scale of "isolated and stacked" MoS_2 slabs does not reflect the entire reality of these materials. It seems more relevant to consider the active phase as a multi-scale arrangement including isolated/stacked slabs and slab aggregates. Anomalous Small Angle X-Ray Scattering (ASAXS) technique has been used by Haubold *et al.*[13–17] for the characterization of heterogeneous

[a] C. Cottrez, Dr. S. Humbert, Dr. A.-S. Gay, Dr. E. Devers, Dr. A. Chaumonnot
IFP Energies nouvelles
Rond-Point de l'échangeur de Solaize BP3
69360 Solaize (France)
E-mail: anne-sophie.gay@ifpen.fr
[b] Dr. F. De Geuser
Univ Grenoble Alpes, CNRS, Grenoble INP, Lab SIMaP
F-38000 Grenoble (France)
[c] Dr. X. Carrier
Sorbonne Université, CNRS, Laboratoire de Réactivité de Surface, LRS
F-75005, Paris (France)

Supporting information for this article is available on the WWW under https://doi.org/10.1002/cctc.202201432

Special Collection *This publication is part of a Special Collection on "French Conference on Catalysis 2022". Please check the ChemCatChem homepage for more articles in the collection.*

catalysts and appears to be suited to estimate the amount and the morphology of the slab aggregates.[12] From the SAXS point of view, the notion of slab aggregates refers to a grouping of molybdenum-containing objects that has a given shape and size. These slab aggregates are therefore distinguished from isolated/stacked slabs only by their different shape and size. Thanks to these novel parameters, Humbert *et al.*,[12] were able to directly relate the intrinsic activity loss to the amount of slab aggregates present within CoMoP/γ-Al_2O_3 catalysts and then demonstrated the relevance of establishing a new multiscale model to describe the influence of the active phase on the catalytic performance.

In the last decades, the influence of the synthesis parameters on the active phase arrangement (at isolated slab scale) and the catalytic activity have been widely studied and very well described. In brief, one of the most common ways to prepare an HDS catalyst is by Incipient Wetness Impregnation (IWI) composed of the following steps:[18,19] i) impregnation of the solution containing the metal precursors onto the support, ii) ageing, iii) drying and iv) sulfidation. Thus, the textural properties[20–25] and the surface reactivity (by the nature of the hydroxyl groups) of the support[26–28] are the first parameters that can influence the arrangement of the active phase. During the impregnation step, the viscosity, the pH,[29–31] the speciation[29,30,32] or the metal loading[1,3,4] of the impregnation solution are also parameters that can influence the Mo arrangement during its contact with the support. In most studies, it has been shown that the ageing step does not influence the arrangement of MoS_2 slabs. However, it does have a clear impact on the nature of Mo particles[33] and on the macroscopic distribution of Mo precursors in the extrudates[22,34,35] which may also influence the catalytic performance. The severity of drying[4,32,36,37] (*e.g.* time, temperature, drying ramp) also appears to be a determining factor. Indeed, the species present in the support can be redistributed and/or precipitate depending on the drying conditions. An optional additivation step can also take place. Thus, the presence of organic additives such as triethylene glycol (TEG) favors the dispersion of isolated/stacked slabs.[12,38–42] In their study, Humbert *et al.*[12] notably showed that additivities had an effect not only on the scale of the isolated and stacked MoS_2 slabs but also on the aggregation state of the slabs. Indeed, the aggregation rate decreases by 50% between non-additivated and TEG-additivated catalysts. Therefore, this demonstrates the relevance of investigating the potential influence of the synthesis parameters onto the multiscale Mo arrangement of Mo (*i.e.* stacked slabs and aggregated slabs) in order to clearly elucidate their impact on the intrinsic activity and raise key parameters to control it.

In this paper, the influence of the ageing and drying steps on CoMoP/γ-Al_2O_3 catalysts will be studied. First, the use of an ageing step or not will give us the opportunity to study drastically different catalysts in terms of macroscopic distribution of metals in the support. Secondly, the drying conditions applied here on the catalysts will also be very different. We will compare the effect of evaporation drying (conventional drying) with sublimation drying (freeze-drying). These two studies will give new insights on the multiscale organization and distribution of the Mo active phase, as well as their impact on the catalytic performance measured by toluene hydrogenation thanks to a multiscale characterization approach (*i.e.* slabs scale, aggregates slabs scale and macroscopic distributions), using XPS, TEM, Electron Probe Micro Analysis (EPMA) and ASAXS techniques.

Results and Discussion

Series of CoMoP/γ-Al_2O_3 catalysts have been prepared by incipient wetness impregnation at different high Mo loadings (18, 22, 26 and 30%wt MoO_3), followed or not by an ageing step (aged (A), not aged (NA)) and conventionally dried in an oven (D) or freeze-dried (FD). Oxide and sulfide catalysts have been characterized at different scales: at the isolated slabs scale by TEM, ASAXS and XPS; at the slab aggregates scale by ASAXS and XPS; at the macroscopic scale by EPMA. More details can be found in the experimental section and the supplementary information (S.I.). Before studying thoroughly the multiscale characterization of the different catalysts, Figure 1 presents the ASAXS curves of the 26%wt MoO_3 sulfided catalysts. Qualitatively, they are clearly different and quantitative information on the isolated/stacked slabs and slab aggregates can be extracted.

Characterizations of the isolated/stacked slabs scale

Figure 2 shows the representative TEM images of the 26 wt% MoO_3 sulfide catalysts. The presence of MoS_2 slabs with a typical layered structure is notable for all catalysts. TEM images of aged catalysts (26_A_D and 26_A_FD catalysts, Figure 2 a and b respectively) are similar for all observed areas, with a very high density of slabs. While for the unaged catalysts (26_NA_FD and 26_NA_D catalysts, see Figure 2 c, d and e, f respectively), the TEM images can be distinguished into two groups: very dense areas, with apparently longs MoS_2 slabs and some "free-slabs" areas. The average stacking and mean slabs length were

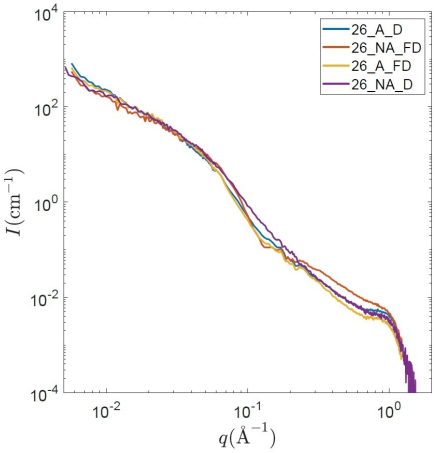

Figure 1. ASAXS $I(E_3)$–$I(E_5)$ curves of the 26 wt% MoO_3 sulfide catalysts.

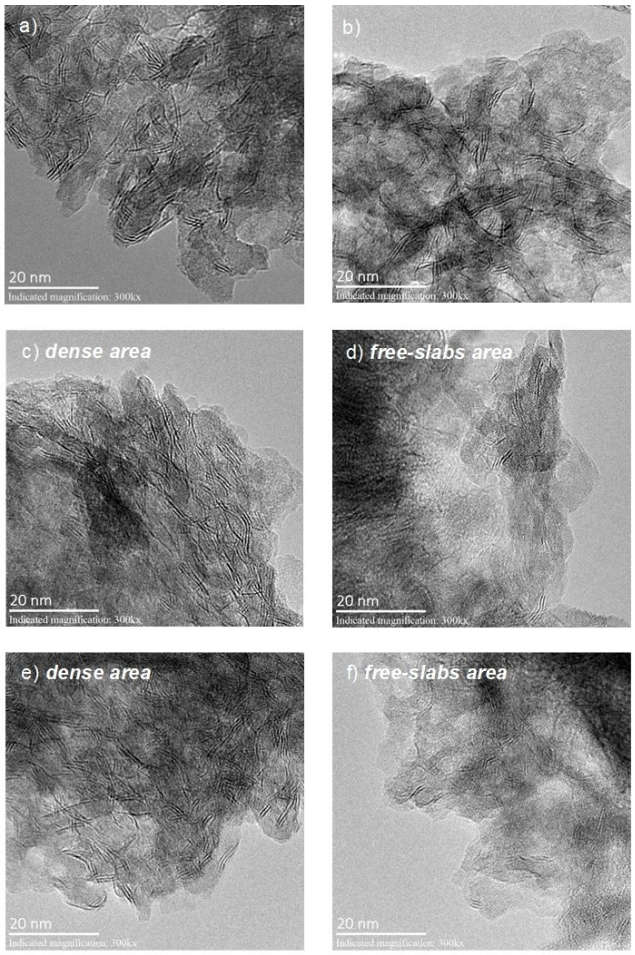

Figure 2. TEM images of a) 26_A_D, b) 26_A_FD, c) and d) 26_NA_FD and e) and f) 26_NA_D sulfide catalysts.

measured by TEM for each sample and are summarized in Table 1 (size and stacking distributions can be found in S.I.). Globally, they appear to be similar for each catalyst, namely double-layered MoS_2 slabs around 3.5 nm long.

However, the slabs characteristics (length: L_{slabs} and stacking: S_{slabs}) can also be collected from ASAXS measurements and are also reported in Table 1. In addition, the slab length distribution obtained for the 26 wt% MoO_3 catalysts are represented on Figure 3. Differences in mean slab length and average stacking are observed between the two techniques (*i.e.* shortest and less stacked MoS_2 slabs for ASAXS measurements compare to TEM ones). Two statements can explain it: i) ASAXS technique distinguishes isolated/stacked slabs from slab aggregates as two different types of objects, while statistical analysis of the TEM images at such high Mo loadings makes it difficult, it is possible that the slabs stacking is overestimated by counting parts of aggregates, ii) TEM technique distinguish MoS_2 slabs longer than 1 nm, which is not the case of the ASAXS technique. Indeed, as ASAXS technique measures the Mo particles diffusion independently from the Mo chemical forms, it might be possible that ASAXS technique measures Mo objects such as single atom-few atoms Mo nanoclusters.[43] Thus, at the larger diffusion vector q, both Mo nanoclusters and MoS_2 isolated/stacked slabs are averaged and lead to a decrease of L_{slabs}.

Hence, while TEM does not seem to be able to distinguish each catalyst, ASAXS appears to be more sensitive and allows to observe differences. First, from a general point of view, for each series, slab length decreases when the MoO_3 loading increases, while the slab stacking tends to increase. For example, for the aged and freeze-dried catalysts (A_FD), L_{slabs} decreases from 2.6 nm to 1.0 nm from 18 to 30 wt% MoO_3. Also, L_{slabs} decreases from 7.1 nm to 2.2 nm from 18 to 22 wt% MoO_3 aged and dried catalysts (A_D). Note that a L_{slabs} of around 7 nm seems unrealistic and must result of the measurement ASAXS signal of a catalyst heterogeneity as discussed in S.I. Secondly, significant length differences can be noticed when comparing the four different series, highlighting the effect of the ageing step and especially the drying on the slab length. Indeed, at same MoO_3 loading (for instance 26 wt% MoO_3), see Figure 3, freeze-drying leads to shorter slabs than drying (1.8 nm and 2.7 nm respectively), and an absence of the ageing step coupled with freeze-drying leads to shorter slab than an aged and freeze-dried preparation (1.3 nm and 1.8 nm respectively). These small mean slabs lengths can translate the presence of numerous Mo nanoclusters.

Table 1. TEM and ASAXS characterizations of the multiscale organization of the sulfide CoMoP catalysts. L_{slabs} is mean slab length (in number), S_{slabs} is the average stacking, C_{ag} is the relative Mo amount (in %) involved in the slab aggregates, *Absolute* C_{ag} is the absolute Mo amount involved in the slab aggregates, $\langle V_{ag} \rangle$ is the mean volume of slabs aggregates and N_{ag}/V_s the aggregate number density.

Sample	TEM Mean Slabs length [nm]	Average stacking	ASAXS L_{slabs} [nm]	S_{slabs}	C_{ag} [%]	*Absolute* C_{ag} [%]	$\langle V_{ag} \rangle$ [nm^3]	N_{ag}/V_s [10^{-6} nm^{-3}]
18_A_D	N/A	N/A	7.1	1.3	67	12	441	70
22_A_D	N/A	N/A	2.2	1.0	57	13	414	84
26_A_D	3.3	2.5	2.7	1.0	51	13	484	86
30_A_D	N/A	N/A	2.1	1.7	58	17	863	68
18_A_FD	N/A	N/A	2.6	1.0	55	10	826	31
26_A_FD	3.7	2.4	1.8	1.9	70	18	2344	24
30_A_FD	N/A	N/A	1.0	1.6	61	18	1652	38
18_NA_FD	N/A	N/A	1.2	1.6	62	11	928	31
26_NA_FD	3.8	2.1	1.3	1.5	52	13	1539	27
30_NA_FD	N/A	N/A	0.9	2.8	87	26	393	225
26_NA_D	3.8	2.4	3.2	1.0	62	16	393	127

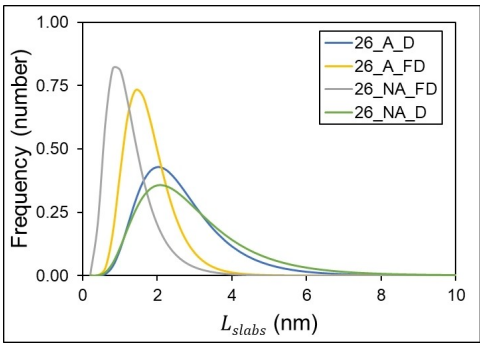

Figure 3. Isolated slabs size distributions (mean slabs length L_{slabs}, in number) of the 26 wt% MoO_3 catalysts obtained from ASAXS measurements.

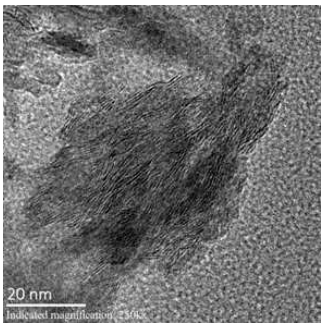

Figure 5. TEM image of a slab aggregate observed in the 26_A_D catalyst.

Concerning the promotion rate by cobalt (*PR*) and the sulfidation rate of Mo ($\%MoS_2$) obtained by XPS, they are given in Table 2. We can notice that each catalyst shows the same *PR* (51–58%) and $\%MoS_2$ around 78%. This shows that neither the ageing, nor the drying steps have an impact on the formation of the MoS_2 phase and its promotion by cobalt, which is in agreement with literature.[12,44]

Characterizations of the slab aggregates scale

The amount of slab aggregates as well as their morphological information can only be obtained by ASAXS characterizations and can be found in Table 1. Overall, the Mo amount involved in the slab aggregates remains roughly constant (relative Mo amount involved in the slabs aggregates C_{ag} between 51% and 62%) independently of the preparation modes, meaning that more than a half of the incorporated Mo is not well dispersed. Thus, no trend is observed concerning the effect of the preparation step or the MoO_3 loading on the aggregation rate (C_{ag}). Only three catalysts present a significantly higher amount of slab aggregates: 18_A_D (67%), 26_A_FD (70%) and 30_NA_FD (87%). Slab aggregates morphology can also be studied thanks to the size distribution (mean aggregate width W_{ag}), in number or in volume, respectively plotted in Figure 4 right and left.

Table 2. XPS results of the sulfide CoMoP catalysts. *PR* is the promotion rate by cobalt and $\%MoS_2$ is the sulfidation rate of Mo.

Sample	Mo/Al atomic ratio	Co/Al atomic ratio	$[\%]MoS_2$	*PR* [%]
18_A_D	0.07	0.03	78	53
22_A_D	0.07	0.03	77	57
26_A_D	0.10	0.04	79	55
30_A_D	0.12	0.05	78	55
26_A_FD	0.12	0.06	79	51
26_NA_FD	0.10	0.06	78	58
30_NA_FD	0.08	0.04	77	52

The mean aggregate width W_{ag} (in volume) ranges from 6.4 to 9.3 nm. Note that the mean aggregate length is proportional to the mean aggregate width W_{ag} and has an order of magnitude of several tens of nm. The presence of such slab aggregates is confirmed by the TEM image presented in Figure 5: an area of 50 by 65 nm with the presence of gathered or intermingled slabs is clearly observed. Such clear images of slab aggregates are rather occasional, so it is difficult to extract morphological information about slab aggregates from the TEM technique.

From the slab aggregates size distributions of the Figure 4, two distinct groups can be distinguished: the freeze-dried samples and the dried samples. As the size distribution are really different, it has been chosen to calculate the mean volume of an aggregate $\langle V_{ag} \rangle$ (see Equation (21)) and then, the aggregate number density N_{ag}/V_s have been calculated also

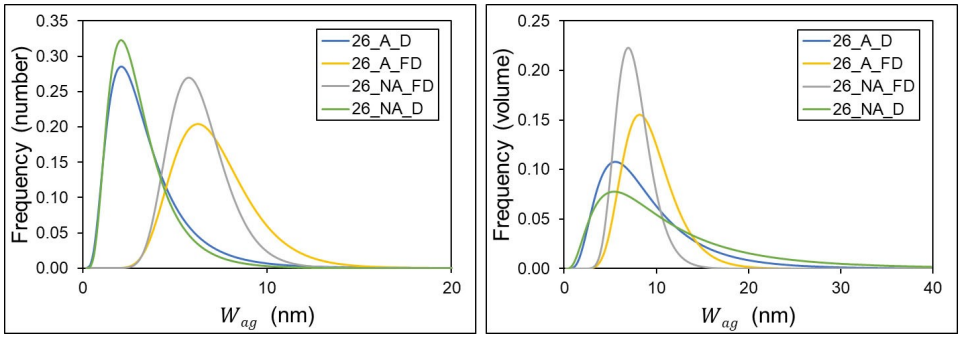

Figure 4. Slab aggregates size distributions (mean aggregate width W_{ag}) of the 26 wt% MoO_3 catalysts, in number (left) and in volume (right).

(Equation (22)) and reported in Table 1. No clear trend is observed concerning the effect of MoO_3 loading on the volume and number of aggregates in each series of catalyst. However, a clear trend is observed when comparing the freeze-dried and the dried catalysts: for instance, at 26% MoO_3 loading and for the aged catalysts, freeze-drying leads to bigger but fewer aggregates (2344 nm^3; 24.10^{-6} nm^{-3}) than drying by evaporation (484 nm^3; 86.10^{-6} nm^{-3}).

Besides, XPS measurements allow to calculate a Mo/Al atomic ratio giving insight of the Mo dispersion on the alumina support surface (Table 2). Focusing on the aged and dried catalysts series (X_A_D), we can see that Mo/Al atomic ratio increases with the MoO_3 loading, which is logical: the more Mo is added, the more quantifiable it is within the support surface. However, the higher the MoO_3 content, the larger the difference between the theoretical Mo/Al ratios and those obtained by XPS measurements as shown in Figure 6. This reflects a dispersion limit of the active phase at the highest contents. This Mo/Al ratio depends on various parameters such as the slab stacking and the Mo aggregation state. It is thus difficult to directly compare it with other characteristics. However, it is roughly in agreement with the slab stacking increase and the *Absolute* C_{ag} (see equation (20)) increase. Moreover, XPS shows a significant drop of Mo/Al ratio for the 30_NA_FD catalyst, which underlines a very poor dispersion of the Mo. This is in good agreement with the aggregate amount C_{ag} (87%) measured by ASAXS. In addition, 26_A_FD presents a high Mo/Al which could be linked to the small slab lengths associated to the presence of Mo nanoclusters.

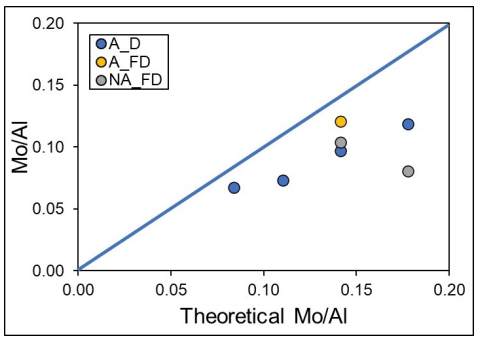

Figure 6. Evolution of the Mo/Al atomic ratios obtained by XPS measurements with the theoretical Mo/Al ratio for the aged catalysts (X_A_D, 26_A_FD, 26_NA_FD and 30_NA_FD).

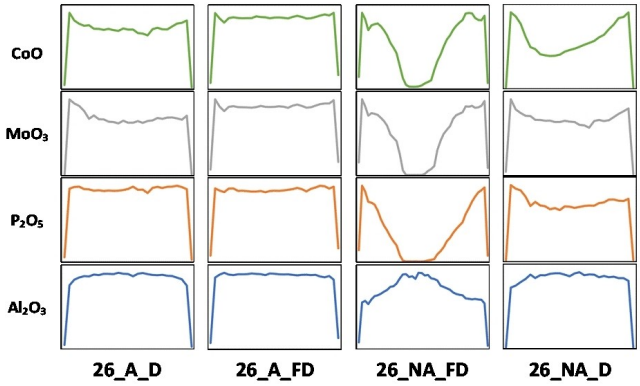

Figure 7. Co, Mo, P and Al metal distribution profiles of 26_A_D, 26_NA_FD, 26_A_FD and 26_NA_D oxide catalysts obtained with EPMA.

Characterizations of the macroscopic extrudates scale

The metals distribution profiles obtained by EPMA on the 26 wt % MoO_3 oxide catalysts are compared in Figure 7. The aged catalysts 26_A_D and 26_A_FD display metal distribution profiles more or less homogeneous, meaning that freeze drying does not deteriorate the metal distribution. The metal distribution profile of sample 26_A_FD is even perfectly homogeneous. However, the absence of an aging step coupled with freeze drying (26_NA_FD) leads to an eggshell profile for Co, Mo and P elements. The shell thickness is 500–600 μm and implies that all charged metals are concentrated there. The use of standard drying, even without ageing (26_A_D and 26_NA_D catalysts), leads to Co & Mo bowl-shaped profiles, which are even more pronounced for 26_NA_D.

These profiles allow to understand the TEM images (see Figure 2) of dense and "free-slabs" areas seen for the not aged catalysts (26_NA_D and 26 NA_FD). It can easily be considered that the dense area corresponds to the edges of the extrudates, highly metals concentrated, when the "free-slabs" area matches with the center of the extrudates.

Catalytic performance

All catalysts were evaluated by toluene hydrogenation and the intrinsic rate constant k' was calculated and compared as a function of MoO_3 wt%, as shown in Figure 8. First, for each series of CoMoP/γ-Al_2O_3 catalysts; the intrinsic rate constant k' tends to decrease with MoO_3 loading. Furthermore, regardless the former parameter (*i.e.* MoO_3 loading) the standard dried catalyst series (X_A_D and X_NA_D) exhibit equivalent catalytic activity. The same observation is made for the freeze-dried catalysts (X_A_FD and X_NA_FD), that are about 1.3 more active than the dried catalysts at the same MoO_3 loading. However, for

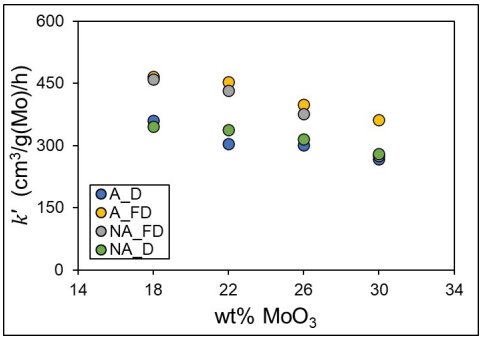

Figure 8. Evolution of the intrinsic catalytic performances (intrinsic rate constant) evaluated by toluene hydrogenation with the wt% MoO_3.

the unaged and freeze-dried series (X_NA_FD), the MoO_3 loading has an even greater impact on the loss of intrinsic activity. Indeed, at the lowest MoO_3 loading, 18_NA_FD catalyst has an intrinsic rate constant k' of 460 cm^3/g(Mo)/h like 18_A_FD catalyst. Then, k' decreases with the MoO_3 loading and falls drastically for 30_NA_FD catalyst (275 cm^3/g(Mo)/h), which corresponds to the same catalytic performances as the dried 30_A_D and 30_NA_D catalysts.

Freeze-drying and drying effect on the arrangement of the active phase

To fully understand the effect of the freeze-drying step on the multiscale Mo organization within the active phase, the aged catalysts from the X_A_D and X_A_FD series are compared.

First, the comparison of the homogeneous metal distribution profile of the 26_A_FD catalyst with the bowl-shaped profile of the 26_A_D catalyst (Figure 7) leads to the following hypothesis: the sublimation of the solvent during freeze-drying prevents any redistribution of the metals within the alumina support, whereas in the case of drying by evaporation, and due to thermal exchanges, the solvent is drained from the center of the extrudate towards the edges. During this phenomenon, only Co and Mo are redistributed, as P shows a strong affinity with Al which avoids any redistribution.[35,45]

ASAXS data show that a sublimation drying (freeze-drying) leads to approximatively 1 nm smaller slabs compared to conventional evaporation drying, but it does not affect the slab stacking. Even though the freeze-drying step affects the isolated slabs morphology, it does not have any influence on the Mo sulfidation degree or promotion rate as shown by XPS results. The presence of such small slabs could be explained by the presence of single atom-few atoms Mo nanoclusters as mentioned before.

In addition to its effect on the slab scale, the drying step also impacts the aggregate scale, not specially on the relative Mo amount involved in the slab aggregates (C_{ag}) that shows no clear trend, but on the aggregate morphology, described by the size distribution presented on Figure 4, by the mean volume $\langle V_{ag} \rangle$ and the aggregate number density N_{ag}/V_s. Freeze-drying leads to the presence of aggregates twice as voluminous as in conventional drying (see Table 1). Consequently, with an approximatively same amount of aggregate, it leads to twice less aggregates per volume unity. All these observations are confirmed by a higher Mo/Al ratio (obtained by XPS) after a freeze-drying (0.12) than after a conventional drying (0.10).

If we consider that the role of the freeze-drying is to block the system right after the ageing step, as observed by EPMA, we can thus take it as a reference to understand the different phenomena involved during a conventional drying step. A growth of the slab occurs, which has the effect to shift the slab size distribution towards larger sizes (see Figure 3, curves grey (26_A_FD) and blue (26_A_D)). Besides, the aggregate volume decreases and the number density of aggregates increases, which highlight a fragmentation of the aggregates, possibly linked to the metal redistribution inside the extrudates.

To summarize (see Figure 9), a conventional drying step allows the growth of isolated slabs and the fragmentation of slab aggregates which leads to numerous and small slab aggregates.

Ageing effect on the arrangement of the active phase

To highlight and understand the influence of the ageing step on the arrangement of the active phase, the freeze-dried catalysts aged (X_A_FD) and not aged (X_NA_FD) can be compared together, such as the dried catalysts, aged (X_A_D) or not aged (X_NA_D).

No significant difference is observed between both dried catalysts. However, it has been demonstrated previously that the drying step had significant effect on the metal distribution, slab length and aggregates morphology. Consequently, the influence of the ageing (or its absence) step is certainly hidden by the drying step that follows. Moreover, part of the ageing could be performed during drying (due to the defrosting of the catalyst that would lead to solvent diffusion). Consequently, it seems obvious that, to evaluate the ageing stage, it is necessary to study the samples (X_A_FD) and (X_NA_FD) having undergone a freeze-drying, which allows to freeze the system in its state.

These two catalysts are drastically different at the macroscopic scale. The egg-shell metal distribution profile obtained by EPMA of the 26_NA_FD (Figure 7) oxide catalyst clearly shows that the ageing step has a role on diffusion of impregnation solution within the support. Without ageing, all the metals added are confined in the 500–600 μm-shell. At the isolated slab scale, the absence of an ageing step leads to smaller MoS_2 slabs (see table 1), particularly at the lowest MoO_3 loading (2.6 nm with ageing and 1.2 nm without ageing). Thus, an ageing step allows the growth or the coalescence of Mo entities that will lead to longer slabs. However, the ageing does not seem to impact the aggregate scale as the aggregate amount (C_{ag}) and morphology ($\langle V_{ag} \rangle$) remain similar. Let's notice that a different behavior is observed for the unaged 30_NA_FD catalyst. At this high loading, the macroscopic metal distribution also affects the isolated and aggregates scale. Indeed, the

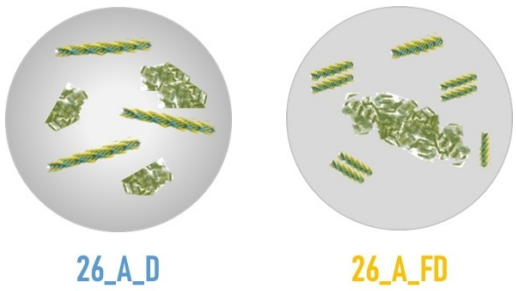

Figure 9. Schematic representation of the effect of freeze-drying on the active phase.

overconcentration of Mo in the shell is such that it limits the good dispersion of Mo, leading to higher stacking (2.8 versus 1.6) and a very high aggregation rate (C_{ag} equals to 87%).

Effect of the multiscale organization of the active phase on the catalytic performance

First of all, it is obvious that the macroscopic metals distribution within the extrudate has no influence on the catalytic performance. Indeed, the freeze-dried catalysts (X_NA_FD and X_A_FD) present drastically different metal distribution profiles (eggshell and perfectly homogeneous profiles respectively). However, these two series both observe very good catalytic performances.

Promotion degree or the Mo sulfidation rate are similar for each catalyst, thus only the multiscale active phase arrangement differs for each catalyst and could possibly explain the different catalytic performances.

The absolute amount of Mo involved in the slab aggregates (*Absolute* C_{ag}) seems to directly control the catalytic performance as shown in Figure 10: the more *Absolute* C_{ag}, the worse the catalytic performance.

A second key parameter was highlighted in the previous sections, such as the mean slabs length. It is then possible to separate the catalysts into two categories: those with slabs of about 1.4 nm, and the others with slabs of about 2.6 nm long. Figure 10 clearly evidences that the presence of smaller slabs is favorable to better catalytic performance. Note that the considered slabs scale might be a mix of small isolated/stacked active phase and ultradispersed Mo nanoclusters. As these catalysts present a higher activity, it means that these Mo nanoclusters are beneficial to the intrinsic activity and hence we could suppose that they are under sulfide forms, in agreement with.[43] STEM-HAADF HR observations could confirm or not the presence of such Mo nanoclusters.

Hence, these two parameters translate two distinct aspects:

- the mean slab length L_{slabs} reflects the fact that the activity is traditionally related to the number of sites situated on the slab edges;[3,10,39]
- the *Absolute* C_{ag} reflects the fact the aggregates are harmful for the catalytic activity, either because the slabs inside these aggregates are hardly accessible, or because they prevent the molecule diffusion inside the catalyst due to pore blocking phenomena. Also, slab aggregates could be less promoted than isolated/stacked slabs due to a poorly dispersed Mo within the oxide phase which induces a low proximity with Co.

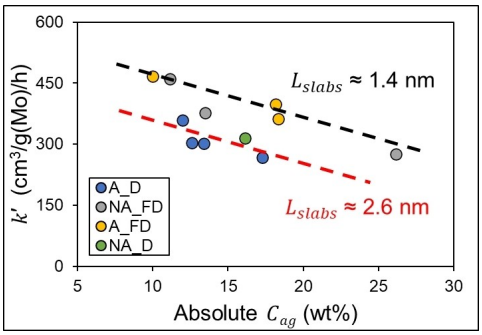

Figure 10. Evolution of the intrinsic catalytic performances evaluated by toluene hydrogenation with the amount of Mo involved in the slab aggregates (***Absolute*** C_{ag})

Conclusion

The aim of this paper was to elucidate the role of the ageing and drying steps on the Mo multiscale arrangement, and to elucidate the impact of the morphological and distribution parameters of the active phase in the catalytic performance.

During the ageing step, the impregnation solution containing the metal precursors diffuse within the support and allows a first growth of the Mo particles that would lead to longer isolated slabs.

The drying step occurs directly after the ageing step and controls the final multiscale Mo arrangement of the active phase. EPMA profiles and XPS measurement show that a redistribution of the metals within the extrudates occurs. This phenomenon is probably due to solvent evaporation. Then, it leads to the growth of isolated slabs and fragmentation of the slab aggregates. The latter will thus be more numerous but smaller.

Combination of the absence of an ageing step followed by a freeze-drying permits to conclude that macroscopic metal distributions (homogeneous or egg-shell profiles) lead to the same catalytic performance except at too high Mo loading. A Mo overconcentration in the shell is detrimental for the Mo dispersion, and for the stacking and aggregation states.

Thanks to all these studies, slabs length (L_{slabs}) and aggregates amount (*Absolute* C_{ag}) have been raised as the key parameters to control the catalytic performance as they control the number of active sites and their accessibility.

Experimental Section

Catalysts preparation

Different series of alumina-supported CoMoP catalysts were prepared by incipient wetness impregnation of mesoporous γ-Al_2O_3 trilobal extrudates (surface area: 273 m^2/g, porous volume (P/P0 max): 0.75 ml/g) with aqueous solutions of MoO_3 (Climax Molybdenum, purity: 99,92%), $Co(OH)_2$ (AXENS, purity: 93%) and H_3PO_4 (VWR, purity: 98%). Each series contained four catalysts with a target amount of 18, 22, 26 & 30 wt% MoO_3 and Co/Mo and P/Mo molar ratios of 0.40 and 0.27 respectively. The impregnated supports were then aged (A) in a water-saturated atmosphere at room temperature overnight or not aged (NA) by freezing them in liquid nitrogen immediately after the fastest possible impregnation (at least, less than 1 minute). The catalysts were finally dried (D) in a stagnant air oven at 120 °C for 5 h, or were freeze-dried (FD) in a freeze-dryer at −60 °C for 20 h.

The catalysts were thus named x_1_2 with × the target amount of MoO_3 in wt%, 1 the ageing step applied (A or NA) and 2 the drying step applied (D or FD).

Catalytic test

The catalytic performance of each catalyst was measured by a toluene hydrogenation reaction using a Flowrence fixed bed reactor (Avantium) containing 16 parallel reactors The catalytic test consisted of two parts: *in situ* sulfidation and the catalytic test itself. The same feed was used for both parts and consisted of dimethyldisulfide (DMDS, 5.9 wt%), toluene (20 wt%) and cyclohexane (74.1 wt%). The total pressure was 60 bar and the hydrogen to feed ratio was 450 NL/L. For the *in situ* sulfidation part, the temperature was increased from RT to 350 °C with a ramp of 2 °C/min and a liquid hourly space velocity (LHSV) of 4 h^{-1}, and maintained for a 1 h-stage. Then, the LSHV is turned down at 2 h^{-1} to start the catalytic test itself at 350 °C. The reaction products were collected at least 6 times each 45 minutes and were analysed by gas chromatography. The toluene-hydrogenation activity k [h^{-1}; Equation (1)], considered as a first-order reaction, was expressed as:

$$k = \ln\left(\frac{1}{1-x}\right) \tag{1}$$

the percentage conversion of toluene in the feed. All the catalytic results will be expressed as the intrinsic rate constant k' [cm^3/g(Mo)/h; Equation (2)], obtained by normalizing k with the mass of MoO_3 loaded in the reactor. k is expressed with an uncertainty of 8%.

$$k' = \frac{k}{gMoO_3/mL} \times 100 \tag{2}$$

The most relevant sulfided used catalysts were selected for an exhaustive characterization.

X-ray Photoelectron Spectroscopy (XPS)

XPS sampling of the sulfide catalysts was performed in a glove box under an argon atmosphere, with controlled oxygen and water levels (less than 20 ppm) to avoid their partial reoxidation. The samples were crushed and pressed onto an indium foil that was attached to the sample holder with double-sided carbon tape. The sample holder was then moved directly into the analysis chamber via the special glove box connection to the XPS spectrometer. XPS spectra of the sulfide catalysts were collected on a Kratos Axis Ultra (Kratos Analytical, U.K.) spectrometer equipped with a monochromatic Al Kα source (1486.6 eV), a hemispherical analyser and a 128-channel delay line detector. Measurements were performed at room temperature (RT) under high vacuum (order of magnitude of 10^{-9} torr) in the analysis chamber. The Co 2p, Mo 3d, P 2p, S 2s, S 2p and Al 2p binding energies (BE) were referenced to the C 1s level at 284.6 eV admitted as carbon contamination. XPS data in the form of relative atomic percentages were obtained by integrating the areas of the corresponding peaks and using relative sensitivity factors given by the manufacturer via CasaXPS software. The Mo/Al and Co/Al surface atomic ratios, Mo sulfidation rate $\%MoS_2$ [Equation (3)] and promotion rate PR [Equation (4)] were calculated as follows:

$$\%MoS_2 = \frac{C_{MoS_2}}{C_{MoS_2} + C_{Mo(VI)} + C_{Mo(V)}} \times 100 \tag{3}$$

$$PR = \frac{C_{CoMoS}}{C_{CoMoS} + C_{Co(II)} + C_{Co_9S_8}} \times 100 \tag{4}$$

with C the relative atomic percentage of the considered species obtained by XPS.

Transmission Electron Microscopy (TEM)

The sulfide catalysts were ground and dry deposited on a holey carbon copper grid. Measurements were performed on a JEOL 2100F TEM operated at 200 kV in high resolution bright field mode with an ULTRASCAN 1000 camera with CCD sensors. The slab length and their stacking were obtained by measuring at least 200 stacked slabs using an in-house software. Average values were obtained by fitting the distribution profiles with a log-normal distribution law (see S.I.).

Anomalous Small Angle X-Ray Scattering (ASAXS)

Data acquisition and processing were performed according to the method adapted by Humbert *et al.*[12] on CoMoS catalysts. Sulfide extrudates were crushed and put into 1.5 mm diameter quartz capillaries in a glove box. Anomalous small-angle X-ray scattering experiments were performed on the D2AM beamline of the ESRF synchrotron. The scattered intensity was measured slightly below the molybdenum K-edge of absorption at the five following energies: E_1 (19700 eV), E_2 (19860 eV), E_3 (19940 eV), E_4 (19975 eV) and E_5 (19990 eV). Calibration of the incident beam energy was carried out with a metallic molybdenum foil. Two sample-detector distances (35 mm and 3600 mm) were chosen to cover the largest q range. The scattering images were recorded using a XPAD detector. The acquisition time (180 s) was determined in order not to saturate the detector. Moreover, a homemade beamstop, consisting of 2 copper square-shaped sheets of 50 μm thick, was placed on the detector to decrease the intensity scattered and recorded at small angles.

For 1D reduction, raw data were corrected by a "flat" to remove the beamstop influence, and normalized by the incoming photon flux, transmission and true thickness calculated from the transmission coefficient. A glassy carbon was measured at each energy and for both sample-to-detector distances to calibrate the intensity in absolute units, *i.e.*, as the differential scattering cross section per unit volume in cm-1. A correction factor was applied from the ratio of the NIST data to the experimental data.

The theoretical aspects of ASAXS technique are exhaustively written in S.I. of this paper, so only the main details are sum up here. Considering a homogeneous matrix including randomly oriented particles with identical shape and with size parameterized by R, the SAXS scattered intensity is defined by Equation (5):

$$I(q) = \frac{N_p}{V_s}\,\Delta\rho^2 \int_0^\infty P(R)V(R)^2|F(q,R)|^2\Psi(q,R)\mathrm{d}R \tag{5}$$

Where N_p the number of particles, V_s the sample volume, $P(R)$ the size distribution function, $F(q,R)$ the form factor, $\Psi(q,R)$ the structure factor which equals to 1 when the particles are well spaced, *i.e.* when distances between particles are larger than particle sizes, and $\Delta\rho^2$ the contrast factor such as Equation (6):

$$\Delta\rho^2 = \left(\rho_p - \rho_m\right)^2 \tag{6}$$

ρ_p and ρ_m the scattering length densities of the particles and the matrix [Equation (7)]:

$$\rho = r_e \sum_j n_j f_j \tag{7}$$

n_j the number density of the atom j in the matrix or in the particles, f_j the atomic form factors and r_e the classical Thomson radius ($r_e =$ 0.282 10^{-12} cm).

In the present case, HDS catalysts are composed of metal particles supported on a porous alumina support. The pores of the latter will contribute significantly to the SAXS signal making it impossible to distinguish the nanoparticles. Therefore, the ASAXS signal can be obtained by subtraction method.[13–17] It consists in subtracting the SAXS intensities obtained at two different energies to avoid the contribution of the porous support. Thus, the resulting intensity is a function of the particles scattering as expressed in Equation (8). Here, the incident beam energy has been varied close to the molybdenum K-edge of absorption as previously described.

$$\langle I(q,E_i)\rangle - \langle I(q,E_j)\rangle = n_p^2 r_e^2 \left(|f_p(E_i)|^2 - |f_p(E_j)|^2\right). \left(S_{pp}(q) + \alpha S_{sp}(q)\right) \tag{8}$$

Where $\alpha = \frac{n_s}{n_p}\frac{f_s}{\overline{f_p}}$ and $\overline{f_p} = \frac{f_p(E_i)+f_p(E_j)}{2}$ is the mean value of $f_p(E)$.

Considering independent spherical metallic particles of radius R_p deposited on a spherical support particle of radius R_s, it is possible to write $S_{pp}(q)$, and $S_{sp}(q)$ as follows [Equations (9) and (10)]:

$$S_{pp}(q) = \frac{N_p}{V_s} \int_0^{+\infty} P_p(R_p) V_p^2(R_p) F_p^2(q,R_p) dR_p \tag{9}$$

$$S_{sp}(q) = \frac{N_p}{V_s} \iint_0^{\infty} P_p(R_p) P_s(R_s) V_p(R_p) V_s(R_s) F_p(q,R_p) F_s(q,R_s) \frac{\boldsymbol{sin}\left(q(R_p+R_s)\right)}{q(R_p+R_s)} \mathrm{d}R_p \mathrm{d}R_s \tag{10}$$

In the present case, $\alpha \sim 0.83$ so the interference term S_{sp} is maybe not negligible. Both terms will be considered the data modeling.

To evaluate the size distribution of the sulfided slabs, a nonlinear least-squares adjustment of the ASAXS I(E_3) - I(E_5) signal is performed on Equation (8). ASAXS I(E_3) - I(E_5) curve shows two inflections of the scattered signal as seen in Figure 11, consequently, two types of molybdenum objects had to be considered. These two populations were attributed to isolated slab at a smaller scale and moderately dense slab aggregates at a larger scale, thanks to electron microscopy observations. Stacked slabs were modeled as discs of height $2H$ and radius R_p, with form factor F_{disc} (q, R_p, H) and volume V_p (R_p, H), and slab aggregates as ellipsoids of revolution (a spheroid) of axes R_{ag}, R_{ag} and νR_{ag} with form factor $F_{ellipsoid}$ (q, R_{ag}, ν) and volume V_p (R_{ag}, ν). The size distributions of stacked slabs and slab aggregates are represented by the log-normal distribution in Equation (11):

$$P_k(R_k) = \frac{1}{\sqrt{2\pi}R_k\sigma_k} \exp\left(-\frac{(\ln R_k - \mu_k)^2}{2\sigma_k^2}\right) \tag{11}$$

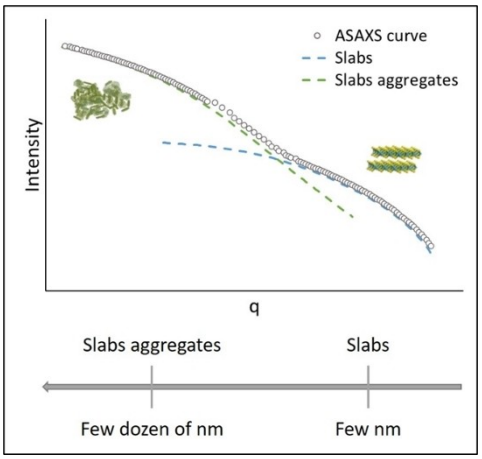

Figure 11. ASAXS I(E_3) - I(E_5) curve processing and multiscale Mo organization modelling

Where k equals to p for isolated slab and to ag for the aggregates, and μ and σ are respectively the scale and the shape parameters of the lognormal law.

The interference between the alumina support and molybdenum phase $S_{sp}(q)$ described in equation (10) must be considered. Therefore, the size distribution $P_s(R_s)$, the particle volume $V_s(R_s)$ and the form factor $F(q,R_s)$ must be defined.

Finally, considering the first population of Mo particles as isolated/stacked slabs and the second one as aggregates of partially dense slabs, it is possible to write the Equation (8) such as (*cf.* S.I for more details) [Equation (12)]:

$$\langle I(q,E_i)\rangle - \langle I(q,E_j)\rangle = w_{\mathrm{Mo_x}} \times w_p \times \frac{\rho_s}{\rho_{\mathrm{Mo_x}}} \times \Delta^2_{\mathrm{Mo_x}}(E_i,E_j) \times \left(S'_{pp} + \alpha S'_{sp}\right) \tag{12}$$

With $M_{Mox} = MoS_2$ in the case of sulfided molybdenum and $M_{Mox} = MoO_y$ in the case of oxide molybdenum, ρ_{Mox} the density (g/cm^3) of the molybdenum phase, w_p and w_a are the fraction of molybdenum involved in the isolated/stacked slabs or slab aggregates, respectively, and $\langle V_p\rangle$ and $\langle V_a\rangle$ are the mean volumes of the isolated/stacked slabs and slab aggregates, w_{Mox} the weight concentration of the molybdenum phase (wt%), ρ_s the sample structural density (g/cm^3) and where [Equation (13)-(15)]:

$$\Delta^2_{\mathrm{Mo_x}}(E_i,E_j) = r_e{}^2 \times \left[\left(n_{\mathrm{Mo_x}} f_{\mathrm{Mo_x}}(E_i)\right)^2 - \left(n_{\mathrm{Mo_x}} f_{\mathrm{Mo_x}}(E_j)\right)^2\right] \tag{13}$$

$$S'_{pp}(q) = \begin{bmatrix} \frac{1}{\langle V_p\rangle} \int_0^{+\infty} P_p(R_p)\, V_p^2(R_p,H) F^2_{disc}(q,R_p,H)\mathrm{d}R_p + \\ \frac{w_a(1-\varepsilon_a)}{w_p} \times \\ \frac{1}{\langle V_a\rangle} \int_0^{+\infty} P_a(R_a) V_a^2(R_a,\nu) F^2_{ellipsoid}(q,R_a,\nu)\mathrm{d}R_a \end{bmatrix} \tag{14}$$

$$S'_{sp}(q) = \left[\frac{1}{<V_p>}\iint_0^\infty P_s(R_s)V_s(R_s)F_s(q,R_s)P_p(R_p)V_p(R_p,H)F_{disc}(q,R_p,H)\frac{\sin\left(q(R_p+R_s)\right)}{q(R_p+R_s)}dR_pdR_s + \frac{w_a(1-\varepsilon_a)}{w_p}\times\frac{1}{<V_a>}\iint_0^\infty P_s(R_s)V_s(R_s)F_s(q,R_s)P_a(R_a)V_a(R_a,\nu)F_{ellipsoid}(q,R_a,\nu)\frac{\sin\left(q(R_a+R_s)\right)}{q(R_a+R_s)}dR_adR_s\right] \quad (15)$$

This model allows the estimation of several morphological characteristics. Particularly, two parameters have been used to describe the isolated slabs:

The mean slab length L_{slabs} (in number) such as Equation (16):

$$L_{slabs} = 2 \times R_p \quad (16)$$

The average stacking S_{slabs} such as Equation (17):

$$S_{slabs} = 0.5 \times \frac{2H}{3.1} + 0.5 \quad (17)$$

3.1 Å is the thickness of a slab according to crystallography. The number averaged length is considered here so that it could be easily compared to the mean length measured in TEM.

Five parameters are useful to describe the slab aggregates:

The mean aggregate width (in volume) W_{ag} such as Equation (18):

$$W_{ag} = 2 \times R_{ag} \quad (18)$$

The relative Mo amount (in %) involved in the slab aggregates C_{ag} such as Equation (19):

$$C_{ag} = \frac{w\varepsilon}{1+w\varepsilon} \times 100 \text{ and } w\varepsilon = \frac{w_{ag}\left(1-\varepsilon_{ag}\right)}{w_p} \quad (19)$$

where w_{ag} and w_p are respectively the molybdenum fraction involved in the slab aggregates and in the isolated slabs, ε_{ag} is the porosity.

The absolute Mo amount involved in the slab aggregates *Absolute* C_{ag} such as Equation (20):

$$Absolute\ C_{ag} = C_{ag} \times w_{Mo_x} \quad (20)$$

where w_{Mo_x} the amount of MoO_3 by weight (wt%).

The mean volume of slab aggregates $\langle V_{ag}\rangle$ (in nm^3) such as Equation (21):

$$\langle V_{ag}\rangle = \frac{4}{3} \times \pi \times \exp\left(3\mu_{ag} + \frac{9\sigma_{ag}^2}{2}\right) \times \nu \quad (21)$$

The aggregate number density N_{ag}/V_s such as Equation (22):

$$\frac{N_{ag}}{V_s} = \frac{w_{Mo_x} \times \rho_s}{\rho_{Mo_x}} \times w_{ag}\frac{1}{1-\varepsilon} \times \frac{1}{\langle V_{ag}\rangle} \quad (22)$$

Where ρ_s the structural density of the sample in g/cm^3 and ρ_{Mo_x} the structural density of the MoS_2 active phase in g/cm3.

Standard errors of ASAXS technique are estimated and discussed in S.I.

Electron Probe Micro Analysis (EPMA)

Oxide catalysts were embedded in a pre-polymerized epoxy resin, then polished and metallized with a thin carbon coating to prevent charging effects. Measurements were performed on the JEOL 8100 microprobe at 20 keV, equipped with 5 WDS detectors. Al, Co, Mo, P concentrations were quantified using the Kα II, Kα I, Lα I and Kα I lines respectively. Metal distribution profiles were carried out by measurements every 50 μm along an extrudate section.

Acknowledgements

ASAXS experiments were performed on BM02-CRG beamline at the ESRF. We are grateful to the beamline staff for smoothly running the facility. We would like to also thank Estelle Péan, Hedwige Poncet, Saloua Sahal-El Ahrache and Dr. Christèle Legens for their contribution in catalysts preparation, EPMA and XPS analysis, respectively.

Conflict of Interest

The authors declare no conflict of interest.

Data Availability Statement

The data that support the findings of this study are available from the corresponding author upon reasonable request.

Keywords: aggregates · ASAXS · $CoMoP/Al_2O_3$ · drying · hydrodesulfurization

[1] P. Platanitis, G. D. Panagiotou, K. Bourikas, C. Kordulis, J. L. Fierro, A. Lycourghiotis, *J. Mol. Catal. A* **2016**, *412*, 1–12.
[2] Z. Liu, W. Han, D. Hu, S. Sun, A. Hu, Z. Wang, Y. Jia, X. Zhao, Q. Yang, *J. Catal.* **2020**, *387*, 62–72.
[3] M. Nikulshina, A. Kokliukhin, A. Mozhaev, P. Nikulshin, *Cataly. Commun.* **2019**, *127*, 51–57.
[4] P. Afanasiev, *Appl. Catal. A* **2017**, *529*, 10–19.
[5] P. Raybaud, J. Hafner, G. Kresse, S. Kasztelan, H. Toulhoat, *J. Catal.* **2000**, *189*, 129–146.
[6] H. Topsøe, B. S. Clausen, F. E. Massoth (Eds.), *Hydrotreating Catalysis*, Springer Berlin Heidelberg, **1996**.
[7] H. Topsøe, B. S. Clausen, R. Candia, C. Wivel, S. Morup, *J. Catal.* **1981**, *68*, 433–452.
[8] H. Topsøe, N. Y. Topsøe, *J. Catal.* **1983**, *84*, 386–401.
[9] A. D. Gandubert, E. Krebs, C. Legens, D. Costa, D. Guillaume, P. Raybaud, *Catal. Today* **2008**, *130*, 149–159.
[10] A. Gandubert, PhD thesis, Université des sciences et technologies de Lille (FR), **2006**.
[11] M. Høj, K. Linde, T. K. Hansen, M. Brorson, A. D. Jensen, J.-D. Grunwaldt, *Appl. Catal. A* **2011**, *397*, 201–208.
[12] S. Humbert, E. Devers, C. Lesage, C. Legens, L. Sorbier, F. de Geuser, V. Briois, *J. Catal.* **2021**, *395*, 412–424.
[13] H.-G. Haubold, T. Vad, N. Waldöfner, H. Bönnemann, *J. Appl. Crystallogr.* **2003**, *36*, 617–620. .
[14] H.-G. Haubold, X. H. Wang, *Nucl. Instrum. Methods Phys. Res. Sect. B* **1995**, *97*.
[15] H.-G. Haubold, X. H. Wang, G. Goerigk, W. Schilling, *J. Appl. Crystallogr.* **1997**, *30*, 653–658.
[16] H.-G. Haubold, X. H. Wang, H. Jungbluth, G. Goerigk, W. Schilling, *J. Mol. Struct.* **1996**, *383*, 283–289.

[17] F. Wen et al, *Eur. J. Inorg. Chem.* **2005**, *2005*, 3625–3640.
[18] M. Digne, *Catalysis by Transition Metal Sulfides. Unitary Steps in the Preparation of Hydrotreatment Catalysts*, Technip, Paris, France, **2013**, *2.1.2*.
[19] P. Munnik, P. E. de Jongh, K. P. de Jong, *Chem. Rev.* **2015**, *115*, 6687–6718.
[20] D. Zhang, X.-M. Liu, Y.-X. Liu, Z.-F. Yan, *Microporous Mesoporous Mater.* **2021**, *310*, 110637.
[21] W. Chen, H. Nie, X. Long, M. Li, L. Zhang, D. Li, *Catal. Today* **2021**, *56*, 14172–14181.
[22] R. Prada Silvy, *Catal. Today* **2019**, *338*, 93–99.
[23] D. Zhang, W.-Q. Liu, Y.-A. Liu, U. J. Etim, X.-M. Liu, Z.-F. Yan, *Chem. Eng. J.* **2017**, *330*, 706–717.
[24] J. Chen, J. Mi, K. Li, X. Wang, E. Dominguez Garcia, Y. Cao, L. Jiang, L. Oliviero, F. Maugé, *Ind. Eng. Chem. Res.* **2017**, *56*, 14172–14181.
[25] L. Yang, C. Peng, X. Fang, Z. Cheng, Z. Zhou, *Catal. Commun.* **2019**, *121*, 68–72.
[26] R. Garcia de Castro, E. Devers, M. Digne, A.-F. Lamic-Humblot, G. D. Pirngruber, X. Carrier, *J. Catal.* **2021**, *403*, 16-31.
[27] E. Dominguez Garcia, J. Chen, E. Oliviero, L. Oliviero, F. Maugé, *Appl. Catal. B* **2020**, *260*, 117975.
[28] W. Zhou, L. Yang, L. Liu, Z. Chen, A. Zhou, Y. Zhang, X. He, F. Shi, Z. Zhao, *Appl. Catal. B* **2020**, *268*, 118428.
[29] L. Le Bihan, P. Blanchard, M. Fournier, J. Grimblot, E. Payen, *J. Chem. Soc.* **1998**, *94*, 937–940.
[30] P. Blanchard, C. Lamonier, A. Griboval, E. Payen, *Appl. Catal. A* **2007**, *322*, 33–45.
[31] P. Raybaud, H. Toulhoat, *Catalysis by Tranistion Metal Disulphides. Atomic scale Structures of Mixed Lamellar Sulphides*, Technip, Paris, France, **2013**, *Vol. 1.2*.
[32] J. Bergwerff, M. Jansen, B. Leliveld, T. Visser, K. Dejong, B. Weckhuysen, *J. Catal.* **2006**, *243*, 292–302.
[33] X. Carrier, J.-F. Lambert, S. Kuba, H. Knözinger, M. Che, *J. Mol. Struct.* **2003**, *656*, 231–238.
[34] J. A. Bergwerff, PhD thesis, Universiteit Utrecht (NL), **2007**.
[35] L. G. A. van de Water, J. A. Bergwerff, B. R. G. Leliveld, B. M. Weckhuysen, K. P. de Jong, *J. Phys. Chem. B* **2005**, *109*, 14513–14522.
[36] Y. S. Al-Zeghayer, P. Sunderland, W. Al-Masry, F. Al-Mubaddel, A. A. Ibrahim, B. K. Bhartiya, B. Y. Jibril, *Appl. Catal. A* **2005**, *282*, 163–171.
[37] P. Munnik, N. A. Krans, P. E. de Jongh, K. P. de Jong, *ACS Catal.* **2014**, *4*, 3219–3226.
[38] D. Nicosia, R. Prins, *J. Catal.* **2005**, *229*, 424–438.
[39] V. Costa, B. Guichard, M. Digne, C. Legens, P. Lecour, K. Marchand, P. Raybaud, E. Krebs, C. Geantet, *Catal. Sci. Technol.* **2013**, *3*, 140–151.
[40] V. Costa, K. Marchand, M. Digne, C. Geantet, *Catal. Today* **2008**, *130*, 69–74.
[41] A. Nuzhdin, G. A. Bukhtiyarova, A. A. Porsin, I. P. Prosvirin, I. V. Deliy, V. A. Volodin, E. Y. Gerasimov, E. N. Vlasova, V. I. Bukhtiyarov, *Catalysts* **2019**, *9*, 96–107.
[42] T. S. Nguyen, S. Loridant, L. Chantal, T. Cholley, C. Geantet, *Appl. Catal. B* **2011**, *107*, 59–67.
[43] D. Ryaboshapka, L. Piccolo, M. Aouine, P. Bargiela, V. Briois, P. Afanasiev, *Appl. Catal. B* **2022**, *302*, 120831–120842.
[44] A. Rochet, B. Baubet, V. Moizan, C. Pichon, V. Briois, *C. R. Chim.* **2016**, *19*, 1337–1351.
[45] J. A. R. van Veen, P. A. J. M. Hendriks, R. R. Andrea, E. J. G. M. Romers, A. E. Wilson, *J. Phys. Chem.* **1990**, *94*, 5282–5285.

Manuscript received: November 21, 2022
Revised manuscript received: February 3, 2023
Accepted manuscript online: February 6, 2023
Version of record online: March 2, 2023